Measurement of buried undercut structures in microfluidic devices by laser fluorescent confocal microscopy

Shiguang Li,[1,2,3,*] Jing Liu,[4] Nam-Trung Nguyen,[4] Zhong Ping Fang,[3] and Soon Fatt Yoon[2]

[1]Singapore-MIT Alliance, N3.2-01-36, 65 Nanyang Drive, Singapore 637460

[2]School of Electrical & Electronic Engineering, Nanyang Technological University, Singapore 639798

[3]Singapore Institute of Manufacturing Technology, 71 Nanyang Drive, Singapore 638075

[4]School of Mechanical and Aerospace Engineering, Nanyang Technological University, 50 Nanyang Avenue, Singapore 639798

*Corresponding author: sgli@ntu.edu.sg

Received 6 July 2009; revised 12 October 2009; accepted 21 October 2009; posted 22 October 2009 (Doc. ID 113787); published 11 November 2009

Measuring buried, undercut microstructures is a challenging task in metrology. These structures are usually characterized by measuring their cross sections after physically cutting the samples. This method is destructive and the obtained information is incomplete. The distortion due to cutting also affects the measurement accuracy. In this paper, we first apply the laser fluorescent confocal microscopy and intensity differentiation algorithm to obtain the complete three-dimensional profile of the buried, undercut structures in microfluidic devices, which are made by the soft lithography technique and bonded by the oxygen plasma method. The impact of material wettability and the refractive index (n) mismatch among the liquid, samples, cover layer, and objective on the measurement accuracy are experimentally investigated.

OCIS codes: 100.5010, 100.6890, 120.0120, 120.2830, 120.6650.

1. Introduction

In metrology, characterizing the undercut microstructures in three dimensions is a challenging measurement task. The characterization process becomes more challenging if the structure is buried. Recently, microfluidic devices have gained more and more attention due to their promising applications in biology [1], optics [2], and many other areas [3]. In the production of such devices, microstructures may become undercut and some defects may occur on the steep sidewalls if the process is not properly controlled, especially when the production involves the photolithography technique of thick-film resists [4–11]. As a microfluidic device must be bonded to a cover layer, the microstructures are naturally buried and their geometry may be further deformed during bonding [12–15]. On the one hand, it is important to characterize such structures to fully understand the manufacturing process for process control. On the other hand, the exact measurement of the buried microstructures is helpful to explain and understand many physical phenomena of microfluid in a deterministic way [16–21]. For example, the distortion of the microchannel's cross section may change the flow condition or even block the flow [21].

To characterize such buried microstructures, optical microscopy [4,12,13,22] or scanning electron microscopy (SEM) [6,7,9,10,14,15,23–25] is often used after physically cutting the device to expose a cross section. The critical dimensional (CD) SEM [26–28]

0003-6935/09/336432-10$15.00/0

and CD atomic force microscope (AFM) [29–33] are also popular for nondestructive three-dimensional (3D) measurements when the structures are open. In addition, some special techniques are applied for some special undercut, open structures, such as scatterometry for periodic grating structures [5,34,35], 3D laser vision systems based on the optical triangulation principle for protruding features [36], laser-based photothermal imaging systems for gold coating samples [37], the optical microscopic image combing chromatic waveguide model for qualitative characterization of the undercut structures [38], the sensing method of measuring the resistance change of embedded N-doped silicon resistors [39], or the alpha particle energy loss method [40]. Unfortunately, most of the above technologies are not capable of measuring buried, polymeric, nonperiodic microfluidic devices that do not have alpha particles or embedded silicon resistors. The only applicable method is the cross-sectional imaging method with optical microscopy or SEM [4,6,7,9,10,12–15,22–25]. Although x-ray computed tomography [41] and ultrasonic imaging [42,43] have been applied to inspect internal structures in the plastics industry or the semiconductor industry, their poor measurement accuracy limits their wide applications for microfluidic devices.

Laser fluorescent confocal microscopy was found to calculate the volume and surface area [44] or to obtain the surface profile [45] from the 3D volume fluorescent image by using the fixed intensity threshold algorithm. However, this algorithm was proved as unreliable for obtaining accurate results [46]. Guilak [44] also acknowledged that the changes in intensity threshold significantly altered the absolute values obtained, which contradicts with the common knowledge that the volume or area of an object should not be determined by the threshold algorithm in software. In fact, the adaptive intensity threshold has to be applied to extract an accurate result, as discussed in our previous work [46]. Exactly speaking, the profiled surface is at positions of maximum intensity variation. By applying the intensity differentiation algorithm with an in-house developed topography software, the positions with maximum intensity variations were found. Challenging features, such as steep sidewalls, were successfully obtained with submicrometer measurement accuracy and repeatability. The possibility of measuring the buried, undercut structures was also discussed in our previous paper. However, due to the lack of practical undercut samples, no meaningful results were obtained. Because of the lack of small features in the range of micrometers or less, the impact of a material's wettability on the measurement results, which is the main concern for this liquid-assisted technology, was not investigated. In this paper, we adopt for the first time this technology to obtain the complete 3D profile of a buried, undercut microfluidic device, i.e., a micronozzle chip. The production process of the device is briefly introduced in Section 2. The profile extraction process is discussed in Section 3. Section 4 covers the measurement accuracy analysis. The influence of the material's wettability and the refractive index mismatch (n-mismatch) among the fluorescent liquid, the sample, the cover layer, and the objective are discussed. Finally, in Section 5, the main findings of this paper are presented.

2. Device Fabrications

The micronozzle device, as shown in Fig. 1 [20], was fabricated in polydimethylsiloxane (PDMS, Sylgard 184, Dow Corning) using the soft lithography technique. The photo mask was designed with AutoCAD and printed on a 12.7 cm × 12.7 cm plastic transparency film using a laser printing system with a resolution of 8000 dpi. SU-8 2050 resist as spin coated on a clean 10 cm silicon wafer. The required channel height is 50 μm, and width is 150 μm for the region between the water port and the pressure port, as highlighted by the dashed circle in Fig. 1. A soft-bake process was needed to harden the SU-8 layer. UV exposure was carried out with the transparency mask for 35 s. After being developed in isopropanol and dried, the negative mold of the channel is left on the wafer. The mixture of PDMS and curing agent was then poured over the fabricated mold. After curing, the PDMS part was peeled off from the mold. Six ports with 0.5 mm diameter were punched with a puncher from the bottom surface on which the channels were printed. The patterned PDMS surface and one piece of glass slide were treated for 30 s at 100 W power with oxygen plasma. Then two of them were immediately brought in contact. To strengthen the bonding quality, the sample was placed into an oven for 15 min at 80 °C. The heat treatment also ensured the hydrophobic recovery of the PDMS surface, which was essential for the formation of water-in-oil droplets [19]. To observe its general geometry,

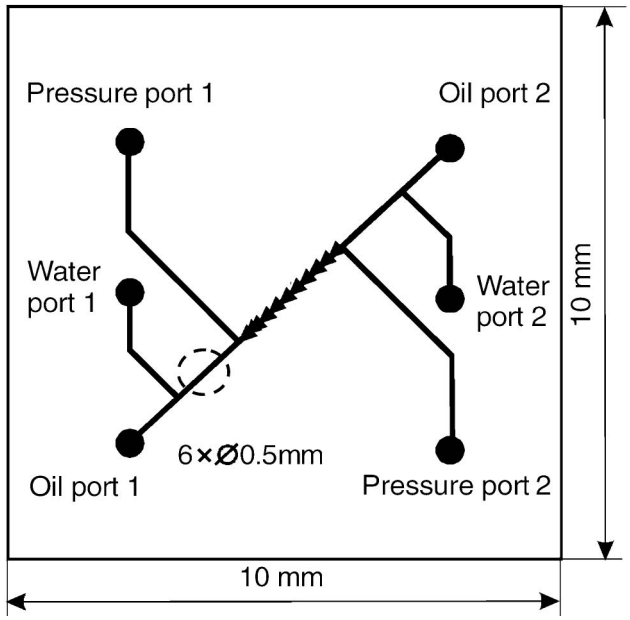

Fig. 1. Illustration of micronozzle chip [20].

another open chip peeled from the same mold was physically cut. The cross-sectional image at the circled region in Fig. 1 is shown in Fig. 2. Evidently, the channel becomes undercut, and the actual depth is more than the expected value of 50 μm. In this paper, we will not analyze why such an irregular shape is made or why the depth deviation is so great, but will focus on how to characterize such geometry without the need for physical cutting as accurately as possible.

3. Device Characterization

To nondestructively obtain the complete profile of the bonded micronozzle chip, deionized (DI) water mixed with fluorescent dye (Fluorescein disodium salt $C_{20}H_{10}Na_2O_5$, Acid Yellow 73 or composite index 45350) was filled into the chip by injecting the liquid from the inlet with a syringe. The sample was then placed on a laser fluorescent confocal microscope (Zeiss LSM510) and scanned layer by layer. The objective in use was Plan-Apochromat 63×/1.4 oil differential index contrast ($n_{oil} = 1.5163$).

Before the scanning process, the contrast of the fluorescent image and the image offset were carefully adjusted so that the interface between the measured sample and the liquid was evident. Ideally, the background signal is slightly greater than zero, and the maximum signal around the interface is slightly less than the saturation value. If the microchannel is very deep, the fluorescent image at the deeper position will become dark, which may be caused by the light transmission ratio, optical aberrations, or the heterogeneous fluorescence density. In this case, the sample can be scanned for several periods at different depth ranges, and the image contrast and offset can be adjusted separately. Series of fluorescent images were obtained after the scanning process, one of which is shown in Fig. 3(a). The bright region is the fluorescent region, and the dark region is the measured sample. The interface between the sample and the fluorescent liquid is the surface to be profiled. The 3D volume image of the measured sample was reconstructed in the topography software written in MATLAB, where a 3D matrix represented the 3D volume image. The cross-sectional image of the chip directly from measurements is shown in Fig. 3(b). In this particular experiment, the sample was scanned for two periods, so there is an intensity step at a depth of about 80 μm. The geometry of the undercut channel becomes evident in Fig. 3(b). According to [46], the profiled surface is at the position where the gradient intensity is the maximum. The 3D matrix in the topography software was thus differentiated along the width direction to achieve the 3D profile of the two sidewalls. Figure 3(c) shows the differentiation image of Fig. 3(a). There are two evident lines. The lower brighter one represents the left sidewall, while the upper darker one represents the right sidewall. By finding the series of positive differentiation peak positions at each pixel in length in every image, the profile of the left sidewall was obtained in Fig. 4(a). The right sidewall profile was similarly obtained by finding the negative differentiation peak positions, as shown in Fig. 4(b). The pseudocolor in the profile represents the width value. During the profile extraction, a variety of denoising algorithms have to be applied, as the extracted profile is quite sensitive to the signal-to-noise ratio of the 3D volume image [46].

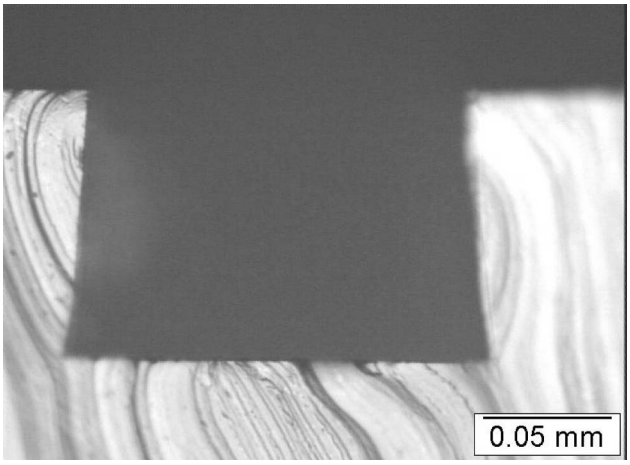

Fig. 2. Cross-sectional image at the circled region in Fig. 1.

1. Smoothing the 3D intensity matrix, because there is evident intensity jump inside the fluorescent region. To avoid the measurement error due to the intensity jump, the digital filter has to be applied. The Gaussian filter is applied because it can preserve edges better than a similarly sized mean filter [47].
2. Setting two suitable intensity thresholds in the intensity matrix. One represents the intensity value inside the fluorescent region, and the other represents the value inside the measured sample. Only the values between these two thresholds remain in the intensity matrix, and these values represent the dataset around the profiled surface.
3. Setting a differentiation threshold, normally zero, in the differentiation matrix. For example, when measuring the right sidewall (the upper wall in Fig. 3(c)], the differentiation peak value must be negative. All the differentiation data greater than zero were removed from the dataset.
4. Filtering out the noise in the end profile with the median filter, because the noise in the geometry profile is often impulse-typed after removing so many data with algorithms 2 and 3. The median filter can keep the geometry edge better than the mean filter for such noise [47,48].

In the above algorithms, the threshold zero in 3 is always correct while measuring a certain wall. The window sizes of $3 \times 3 \times 3$ for the Gaussian filter in 1 and 3×3 for the median filter in 4 are often enough to achieve a smoother profile without losing the geometric details. The determination of the intensity thresholds in 2 is slightly complicated. According to the profile extraction principle, only the dataset

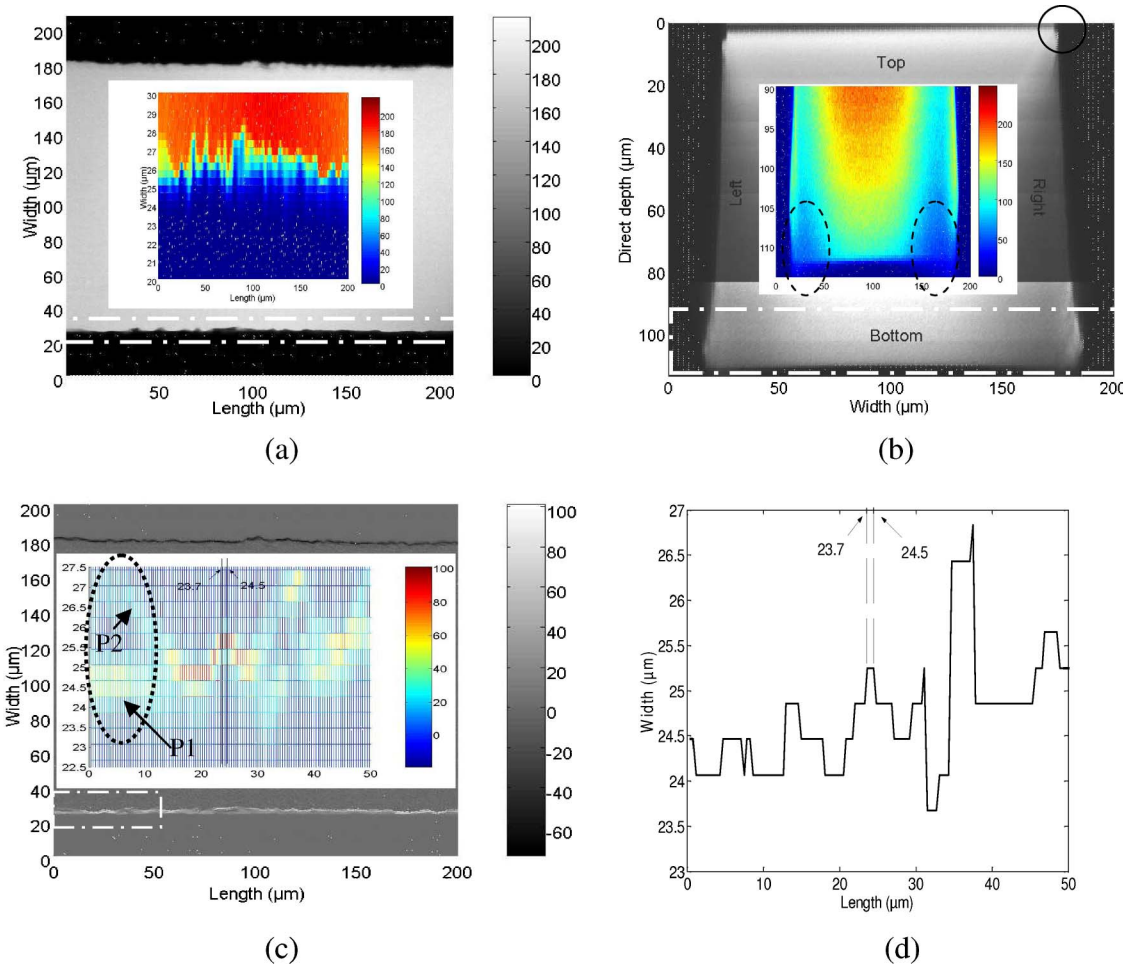

Fig. 3. (Color online) Fluorescent image directly obtained from the laser confocal microscope. (a) Plan view, (b) cross-sectional image, (c) differentiation image of (a). The insets are the enlargement at the region marked with a dashed-dotted square in the respective diagrams. The pseudocolor is displayed for easy observation. (d) Profile of the inset of (c).

around the differentiation peaks is useful. The thresholds have to meet two requirements: (i) they must not filter out the data around the differentiation peaks; (ii) the thresholds should filter out the noninterface data as much as possible to effectively decrease the profile noise. As the intensity values in the fluorescent images vary with depth, estimating the two thresholds with only one image does not suit to the 3D volume image. In practice, the cross-sectional differentiation images in the x–z plane before and after intensity filtering are compared frequently to find the optimum thresholds. With the above process, the 3D top and bottom profiles of the channel were also obtained by doing differentiation along the depth direction, as shown in Figs. 4(c) and 4(d). The color in the profile represents the depth value. Figures 4(a) and 4(b) show that there are rich scratches on the sidewalls. The sidewall geometry variation close to the channel bottom is much more evident than in the other regions. The channel top and the channel bottom are slightly tilted as shown in Figs. 4(c) and 4(d), which will result in the variation of the cross-sectional area along the channel length. The profile quality at the circled regions in Figs. 4(c) and 4(d) is not very good, as is to be discussed in Section 4. The cross-sectional profile along the dashed line is shown in Fig. 4(e). The distance between the channel top and the channel bottom is 107 μm. The widths of the channel top and the channel bottom are 149 and 177 μm, respectively.

4. Measurement Accuracy Analysis

In the measurements, the refractive indices of the cover layer, the sample, the fluorescent liquid, and the immersion medium of the objective are different. In the production of microfluidic devices, the cover layer is often a polymeric material whose thickness and refractive index deviate from the standard parameters of a glass coverslide. If the device is thermally bonded, serious birefringence often occurs in the cover. The n-mismatch inside the measured region will affect the measurement accuracy. As the liquid assists in finding the sidewall information in this technique, the wettability of the material will affect the measurement accuracy, especially when the channel has small defects and sharp corners. This section will experimentally investigate how these two factors affect the measurement accuracy.

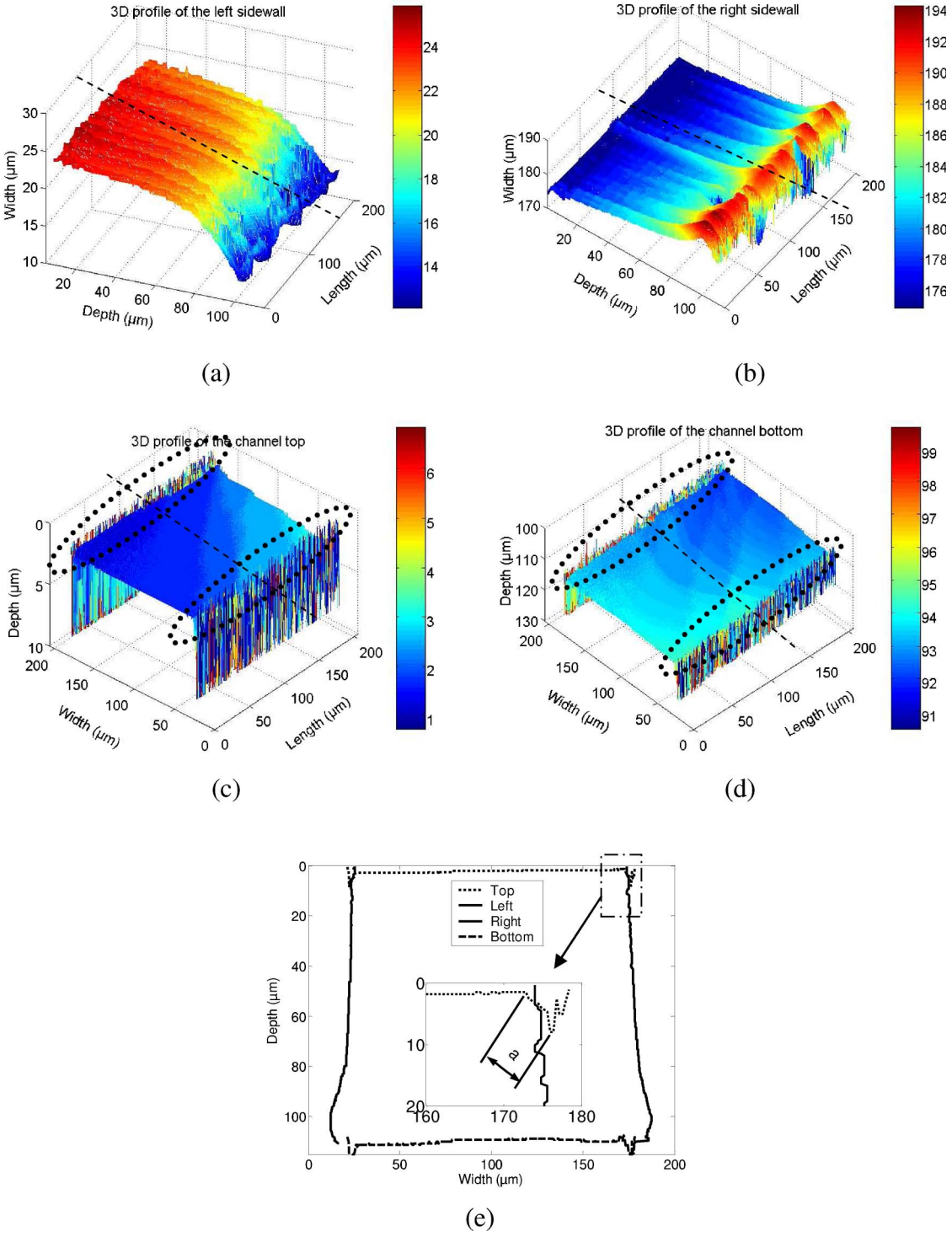

Fig. 4. (Color online) Three-dimensional profiles of the four walls of the buried channel. (a) Left, (b) right, (c) top, and (d) bottom. Their positions are defined in Fig. 3(b). (e) Cross-sectional profile along the dashed line in (a)–(d). The inset is the enlargement of the right top corner as outlined by the dashed-dotted square.

A. Influence of Refractive Index Mismatch on Measurement Accuracy

The three most evident effects of the n-mismatch are (i) the channel depth is elongated when the light transmits from an optically loose medium to the optically dense medium, or is compressed in the opposite case [49–54]; (ii) the fluorescent image will become darker and the axial resolution will become lower due to the broadening of the point spread function (PSF) [49,52–56]; (iii) the fluorescent image will become blurred when there is serious birefringence inside the cover layer.

The effect of the n-mismatch between two different media with refractive indices n_1 and n_2 in the axial direction has been systematically investigated either by wave optics or geometrical optics [49–58]. The conclusions in the investigation are suitable for measuring the channel depth if the cover layer is a piece of standard coverslide. In general, if we denote the ratio between the actual channel depth (ACD) and the direct channel depth (DCD) as the axial scaling factor (ASF), the ASF is not the same as the paraxial estimate: n_2/n_1 when the light transmits from the medium with n_1 to the medium with n_2. Despite that there are some slight discrepancies among different simulation models, the possible factors that may affect the ASF value are summarized as the refractive indices of media [49–56], the direct channel depth [52,54], the numerical aperture of the objective [50,52], the pinhole size [54], and the magnification [54]. The other factors, e.g., the wavelength [57], state of polarization [52], and focal length [58], have no evident relationship with the ASF, as we also simulated with the geometrical optics model independently and achieved the same conclusions. The ASF is slightly greater than the paraxial estimate when $n_1 < n_2$, and slightly less than the paraxial estimate when $n_1 > n_2$ [49,50,52,54]. As the cover layer in microfluidic devices is often made with thick polymeric material, such as polymethyl methacrylate (PMMA) or PDMS, additional optical aberrations caused by the cover layer may cause more ASF deviation from the paraxial estimate, more PSF broadening, and may even make the ASF polarization sensitive. From the above brief summary, it can be seen that the depth recovery depends on many factors, and the paraxial estimate may not be accurate enough. In experiments, we obtained the ASF value by measuring an open channel with this system and an optical 3D profiler (Veeco NT3000). Before measuring the open channel with this system, some fluorescent liquid was dripped onto the open channel and a piece of cover layer identical to that for the buried chip covered the open channel. The channel depth obtained from the 3D profiler was regarded as the real depth. The depth ratio from the two measurements was regarded as the ASF in experiments. The buried channel was then measured under the same measurement conditions: the fluorescent liquid, objective (numerical aperture and magnification 1), zoom lens (magnification 2), pinhole size, and laser source (polarization). The depth of the buried channel in Fig. 3 was obtained by multiplying the direct depth by the experimental ASF value of 0.97 for the oil-immersion objective. The width value was directly read out from the profile and its accuracy was limited by the pixel size of the detector. Although this ASF determination method is quite straightforward, its measurement accuracy is affected by the geometry quality of the open channel and the wettability of material (as is to be discussed in Subsection 4.B). If the measurement accuracy requirement for the buried channel is in the range of submicrometers, the depth variation of the open channel for the ASF determination should be, at most, in the range of several tens of nanometers. As the ASF keeps constant with a 50% object-size variation [53], some height standard whose depth deviates less than 50% from the expected channel depth could be used for the ASF determination. To avoid the influence of the material's wettability, the standard is better made by highly hydrophilic material, such as metals, glasses, or ceramics [59]. Although the depth recovering is complicated, it is not necessary for production control in most cases. In production environments, the relative comparison between samples is much more important. Therefore, the repeatability requirement for the measurement system is stricter. For this system, the measurement repeatability can achieve submicrometers [46]. If the depth needs to be coarsely estimated, the paraxial estimate is enough with a 4% measurement error [52]. We have measured a rectangular silicon step whose depth was $52.34 \pm 0.04\,\mu$m by the above oil-immersion objective with a mechanical scanning step of $0.38\,\mu$m. The liquid was dimethyl sulphoxide, and the Fluorescein was the "reference standard" F-1300 (Invitrogen, USA). The averaged direct depth from experiment was $54 \pm 0.44\,\mu$m over 50 measurements. After multiplying the refractive index ratio between the liquid ($n_2 = 1.4785$ [60]) and the oil ($n_1 = 1.5163$), the measured depth was $52.7 \pm 0.43\,\mu$m. The accuracy was $0.4\,\mu$m, and the standard deviation was $0.43\,\mu$m; both were of the same order of magnitude of the mechanical scanning step.

The darker image caused by the PSF broadening is evident when measuring the deep or the undercut structures. This is because the optical aberrations are more serious under a thick liquid layer or a thick piece of sample layer. Conventionally, the image contrast varies along the depth. In order to extract the profile accurately, it is very critical to make the interface between the fluorescent liquid and the measured sample as evident as possible. Thus, it is necessary to adjust the image contrast and offset at different depths during mechanical scanning or to do additional data processing in software. A special issue should be noted, that the shadows of the real features or defects at the shallower positions can be captured at the deeper positions for the undercut structures. These shadows possibly appear in the profile and it may be wrongly judged as some defects. During the data analysis, the real defects and the feature shadows are to be discriminated according to their different characteristics. For example, there are two narrow lines at the channel bottom, as circled in Fig. 4(d). Their lateral positions are almost the same as those of the two top edges as shown in Fig. 4(e). When observing the fluorescent image at the channel bottom in the inset of Fig. 3(b), the image intensity at the two circled regions is much lower compared to their surroundings. The pseudocolor represents the intensity value in the inset. There is no evident boundary between the "defects" and their

surroundings, indicating that they are not the real defects but are the shadows of the two top edges. On the contrary, on the sidewall regions [the inset of Fig. 3(a)], the intensity variation at the sidewall is very evident and sharp, which indicates that the defects in the sidewall profile are not the shadows. As the shadows are the natural phenomenon in optics and they are often darker than their surroundings, it is easy to identify them in the profile.

To measure microfluidic devices bonded with a thick piece of polymeric material, a special objective designed for different cover thicknesses must be used. The optical objective used in our experiments is a LD-Achroplan 40×/0.6 corr Ph2 (Zeiss, Germany). It is a dry objective. The presumed cover layer material is glass. Figure 5 shows the cross-sectional profile of a buried microchannel made by PMMA. The dashed and solid curves represent the channel top and the channel bottom, respectively. The inset is the raw fluorescent image. The sample was thermally bonded, and the cover layer thickness was about 1 mm. The birefringence of the cover layer can be observed by placing the layer between two pieces of polarizer to observe the polarization interference pattern. The extracted profile is rougher in this case. After removing the cover layer, and measuring the microchannel with a 3D profiler, we discovered that the measured sample is much smoother. The rougher profile is obtained because the one laser spot is divided into two spots due to the birefringence of the cover layer. The received signal is the mean value from a small volume. Despite the birefringence in this paragraph and the n-mismatch in the last paragraph, both of which lead to worse image quality, their effects are different. The mismatch in refractive index mainly results in spherical aberrations. The light deviating from the paraxial focusing depth is the large aperture light, which can be effectively depressed by using the pinhole [54]. So the image affected by n-mismatch is darker. The sharpness at the interface between the measured sample and the liquid is less affected. Instead, if there is birefringence in the cover layer, even the paraxial light cannot focus on a spot. The subsequent effect is that the interface becomes blurred, while the image contrast is less affected. Even though the profile is rougher in this case, one can still expect that the cross-sectional area should be close to that without birefringence because the area calculation exhibits the profile integration effects. If the more accurate dimensional parameters are needed, the mean filter with larger window size is additionally suggested to apply to the profile. The bold line in Fig. 5 is the averaged profile with a Wiener filter whose window size is 20 × 20.

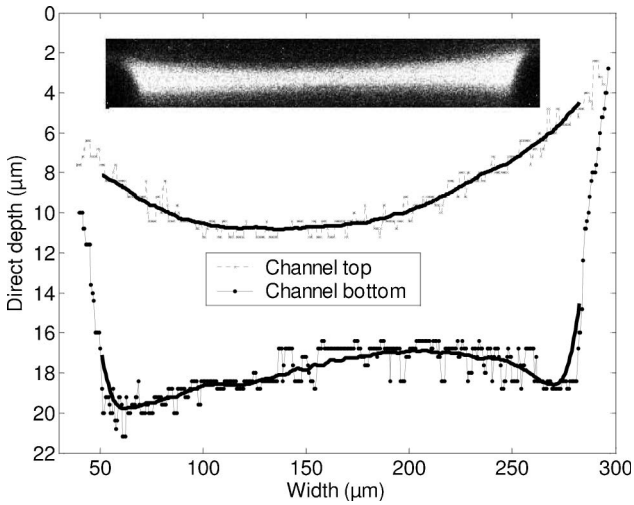

Fig. 5. Cross-sectional profile of a buried channel made by PMMA material and bonded with thermal and pressure method. The inset is the raw fluorescent image.

Another experiment was conducted to measure deep undercut features. As the birefringence inside the cover layer can lead to the interface blurring, the interface at the sidewall may be also blur, because the refractive indices of the sample and the liquid are different. However, the measurement results in Fig. 3(b) show that the sidewall is quite sharp. To examine the sidewall quality for the deep undercut features, an edge of a piece of PDMS substrate was cut at an angle by a sharp blade. The cut device was then inversely placed in fluorescent liquid to simulate the undercut situation. Figure 6 shows its measurement results. The interface still is sharp and evident along the depth. This may be because the light transmitting through the sample has no evident contribution for the image at the interface, as it does not excite too much fluorescent light.

B. Influence of Material Wettability on Measurement Accuracy

As a liquid-assisted technology, the wettability of material plays an important role in measuring the small features, defects or sharp corners. If the liquid is filled into the rough microchannels or in the channels with small grooves, such as defects, there lies "competition" between complete liquid penetration into the rough grooves and entrapment of air bubbles inside the grooves underneath the liquid. The former is the homogeneous wetting regime, while the latter is the heterogeneous wetting regime [61]. In experiments, this phenomenon can be well observed when investigating the small defects on the sidewall. For example, the inset of Fig. 3(c) shows the enlargement of the lower sidewall marked with the dashed-dotted square. The pseudocolor represents the differentiation value. The pixel size of the image is 0.4 μm.

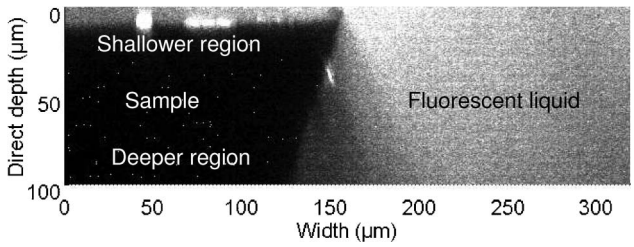

Fig. 6. Cross-sectional image of an undercut feature.

The maximum differentiation values at each pixel in length are not the same. For this technology, the differentiation peak value at the profiled surface is proportional to the fluorescence density inside the laser spot providing the system parameters, such as the spot size, intensity, and others, are the same during measurement [46]. The differentiation peak variation along the length indicates the fluorescence density is heterogeneous at the profiled surface. The circled region shows two evident differentiation peaks for each pixel in length. According to the liquid "competition" theory, the lower peak line (P1), at a width of about 24.5 μm, should represent the interface between the heterogeneous liquid and the measured sample. The higher tilted peak line (P2) should represent the interface where the liquid transits from the heterogeneous regime to the homogeneous regime. If the differentiation peaks at P2 happen to be greater than that at P1, the sample surface would be misjudged. The subsequent result would be that the depth of the small grooves is underestimated. In most cases, the obtained profile is noisy at the small regions. After applying the filter algorithms in the software, the information at these regions will be missing. Even though some information of the small regions may be missing and the defect distribution may be underestimated due to the material's wettability, a part of small defects are possibly found in the profile for qualification analysis. Figure 3(d) is the geometry profile of the inset of Fig. 3(c). There is a small defect between 23.7 and 24.5 μm (two pixels) in the profile. By observing the same region in the inset of Fig. 3(c), it can be found that the differentiation value is greater than zero. This means some liquid penetrates into the small region of 0.8 μm. The measurements indicate the small features or defects with a size of 0.8 μm are possibly found with this technology.

The liquid heterogeneity will also affect the measurement accuracy of sharp corners. Figure 4(c) shows that the profile quality at the two top corners is not good. The inset of Fig. 4(e) shows the enlargement of the cross-sectional profile at the right top corner. The dotted curve and the solid curve, respectively, are the top profile and the sidewall profile obtained by doing differentiation along the depth direction and the width direction. The top profile looks like a triangle, while the sidewall profile appears undercut at this corner. This discrepancy can be well explained with the material's wettability. As the corner is concave, there is air at this region. The fluorescent liquid will become heterogeneous. There possibly are two evident interfaces at the corner according to the discussion in last paragraph. In the experiment, the two interfaces became evident by doing differentiation along the depth, which formed the two edges of the small triangle in the top profile. As the intensity variation at the undercut interface was much more evident, as can be seen at the circled top corner in Fig. 3(b), the differentiation along the width direction just found the undercut interface. With the common knowledge that the interface between the heterogeneous liquid and the measured sample is always deeper than the liquid regime transition interface, the outside edge of the small triangle is the more convincing surface profile. The "a" in Fig. 4(e) is less than 10 μm, indicating that the corner possibly becomes rounder when the corner space is about several micrometers for the hydrophobic PDMS material and the water. The experiments also showed that a varies with the channel size and the material's wettability. To effectively remove away the measurement error caused by the material's wettability, the measured sample is suggested to be placed in the environment with little or no air. Measuring the microchannel before the surface recovery of PDMS also helps to reduce the effect of wettability because the PDMS before recovery exhibits hydrophilic properties [62].

5. Conclusion

In the production of microfluidic devices, the geometry measurement of the buried microstructures is important either for making high-quality products or for understanding the fluid phenomena inside the devices. In this paper, the complete geometry of a bonded, undercut microfluidic device was successfully measured by laser fluorescent confocal microscopy and an intensity differentiation algorithm for what we believe is the first time. In general, for this liquid-assisted technology, it is critical to make the liquid completely contact with the profiled surface. The profile's quality is sensitive to the signal-to-noise ratio in the raw fluorescent images and varied denoising algorithms have to be applied in the profile extraction process. As there is a "competition" between complete liquid penetration into the small regions and entrapment of air bubbles inside the small regions underneath the liquid, not all defects can be obtained in the profile and the corner's sharpness may be underestimated. For the hydrophobic PDMS sample with a depth of 107 μm and a width of 150 μm, the experimental results showed that the 0.8 μm defects were possibly found, and the corner rounding size was several micrometers. The measurable defects and the corner roundness vary with the channel size and the material's wettability. Because the high-spatial-frequency components in the profile are affected by the intensity fluctuation inside the fluorescent image, the wettability of the material, denoising algorithms in the software, and many other factors [46], the extracted surface roughness is not accurate. After filtering out the high-spatial-frequency components with a four-step denoising algorithm, the measurement accuracy of the profile is in the range of submicrometers. The homogeneous n-mismatch in the measured region mainly results in an elongated or a compressed depth value and a broadened PSF, i.e., lower image contrast and worse axial resolution. When measuring the undercut features, feature shadows possibly appear in the extracted profile. As the shadows have no evident interface with their

surroundings, they can be correctly identified during data analysis. Special consideration should be taken when the microchip is thermally bonded or bonded by similar methods, potentially resulting in birefringence inside the cover layer. In this case, the intensity variation around the profiled surface is less evident and the extracted profile is rougher. The fifth denoising algorithm, i.e., the mean filter with larger window size, must be applied to obtain the more accurate profile with the cost of lost of geometry details. The future work is to theoretically analyze the dependence of PSF broadening, polarization sensitivity, and the measurement accuracy of cross-sectional areas of the buried structures on the birefringence, thickness, and refractive index of polymeric cover material when using the dry objective. According to the analysis results, the optimum window size of the mean filter in the fifth denoising algorithm could be determined to ensure the measurement accuracy of channel depth to be in the range of submicrometers. The effects of the n-mismatch in the lateral direction, i.e., inside the image plane, on the measurement results also could be investigated in the future.

References

1. M. Hashimoto, F. Barany, and S. A. Soper, "Polymerase chain reaction/ligase detection reaction/hybridization assays using flow-through microfluidic devices for the detection of low-abundant DNA point mutations," Biosens. Bioelectron. **21**, 1915–1923 (2006).
2. K. Campbell, A. Groisman, U. Levy, L. Pang, S. Mookherjea, D. Psaltis, and Y. Fainman, "A microfluidic 2×2 optical switch," Appl. Phys. Lett. **85**, 6119–6121 (2004).
3. B. Z. Yang and Q. Lin, "A planar compliance-based self-adaptive microfluid variable resistor," J. Microelectromech. Syst. **16**, 411–19 (2007).
4. R. B. Xing, Y. Xuan, Z. Wang, and D. G. Ma, "Undercut structures fabricated by microtransfer printing combined with UV exposure and their applications," Curr. Appl. Phys. **9**, 760–763 (2009).
5. R. M. Al-Assaad, L. Tao, and W. C. Hu, "Visible light angular scatterometry for nanolithography," Proc. SPIE **6518**, 651839 (2007).
6. Y. F. Chen, Z. Q. Lu, X. D. Wang, Z. Cui, G. H. Pan, Y. Zhou, M. Muñoz, C. Hao, Y. H. Lu, and N. Garcia, "Fabrication of ferromagnetic nanoconstrictions by electron beam lithography using LOR/PMMA bilayer technique," Microelectron. Eng. **84**, 1499–1502 (2007).
7. Y. J. Chuang, F. G. Tseng, and W. K. Lin, "Reduction of diffraction effect of UV exposure on SU-8 negative thick photoresist by air gap elimination," Microsyst. Technol. **8**, 308–313 (2002).
8. D. J. D. Carter, A. Pepin, M. R. Schweizer, H. I. Smith, and L. E. Ocola, "Direct measurement of the effect of substrate photoelectrons in x-ray nanolithography," J. Vac. Sci. Technol. B **15**, 2509–2513 (1997).
9. J. L. Lenhart, D. Fischer, S. Sambasivan, E. K. Lin, W. L. Wu, D. J. Guerrero, Y. B. Wang, and R. Puligadda, "Understanding deviations in lithographic patterns near interfaces: characterization of bottom anti-reflective coatings (BARC) and the BARC—resist interface," Appl. Surf. Sci. **253**, 4166–4175 (2007).
10. S. Murakawa and J. P. Mcvittie, "Mechanism of surface charging effects on etching profile defects," Jpn. J. Appl. Phys. **33**, 2184–2188 (1994).
11. Y. Rody, P. Martin, C. Couderc, P. Sixt, C. Gardin, K. Lucas, K. Patterson, C. Miramond-Collet, J. Belledent, R. Boone, A. Borjon, and Y. Trouiller, "Evaluation of transparent etch stop layer phase shift mask patterning and comparison with the single trench undercut approach," Proc. SPIE **5992**, 59920R (2005).
12. B. Samel, M. K. Chowdhury, and G. Stemme, "The fabrication of microfluidic structures by means of full-wafer adhesive bonding using a poly (dimethylsiloxane) catalyst," J. Micromech. Microeng. **17** 1710–1714 (2007).
13. W. W. Y. Chow, K. F. Lei, G. Shi, W. J. Li, and Q. Huang, "Micro fluidic channel fabrication by PDMS-interface bonding," Proc. SPIE **5275**, 141–148 (2004).
14. Y. C. Su and L. W. Lin, "Localized bonding processes for assembly and packaging of polymeric MEMS," IEEE Trans. Adv. Packag. **28**, 635–642 (2005).
15. X. L. Zhu, G. Liu, Y. H. Guo, and Y. C. Tian, "Study of PMMA thermal bonding," Microsyst. Technol. **13**, 403–407 (2006).
16. J. J. Huang, C. Shu, and Y. T. Chew, "Lattice Boltzmann study of droplet motion inside a grooved channel," Phys. Fluids **21**, 022103 (2009).
17. M. H. Khadema, M. Shamsa, and S. Hossainpourb, "Numerical simulation of roughness effects on flow and heat transfer in microchannels at slip flow regime," Int. Commun. Heat Mass Transf. **36** 69–77 (2009).
18. R. Q. Xiong and J. N. Chung, "Investigation of laminar flow in microtubes with random rough surfaces," Microfluid. Nanofluid. (2009), http://www.springerlink.com/content/g7h746461255g4ng/
19. S. H. Tan, S. M. S. Murshed, N. T. Nguyen, T. N. Wong, and L. Yobas, "Thermally controlled droplet formation in flow focusing geometry: formation regimes and effect of nanoparticle suspension," J. Phys. D **41**, 16550 (2008).
20. J. Liu, Y. F. Yap, and N. T. Nguyen, "Behavior of microdroplets in diffuser/nozzle structures," Microfluid. Nanofluid. **6**, 835–846 (2009).
21. M. G. Alonso-Amigo and T. Adams, "Development of a plastic microfluidics chip," IVD Technology, http://www.devicelink.com/ivdt/archive/03/03/003.html (2003).
22. S. J. Paik, J. Kim, S. Park, S. Kim, C. Koo, S. K. Lee, and D. D. Cho, "A novel micromachining technique to fabricate released GaAs microstructures with a rectangular cross section," Jpn. J. Appl. Phys. **42**, 326–332 (2003).
23. J. Li, A. Q. Liu, and Q. X. Zhang, "Tolerance analysis for comb-drive actuator using DRIE fabrication," Sens. Actuators A, Phys. **125**, 494–503 (2006).
24. Y. J. Huang, T. L. Chang, and H. P. Chou, "Study of symmetric microstructures for CMOS multilayer residual stress," Sens. Actuators A, Phys. **150**, 237–242 (2009).
25. C. C. Kao, J. T. Chu, H. W. Huang, Y. C. Peng, C. C. Yu, Y. L. Hseih, C. F. Lin, H. C. Kuo, and S. C. Wang, "InGaN-based light-emitting diode with undercut side wall," in *17th Annual Meeting of the IEEE/Lasers and Electro-Optics Society 2004* (IEEE, 2004), paper TuO4.
26. T. Marschner and C. Stief, "Characterization of 193 nm resist layers by critical dimension-scanning electron microscopy sidewall imaging," J. Microlith. Microfab. Microsyst. **4**, 013007 (2005).
27. B. D. Bunday, M. Bishop, J. R. Swyers, and K. Lensing, "Quantitative profile-shape measurement study on a CD-SEM with application to etch-bias control and several different CMOS features," Proc. SPIE **5038**, 383–395 (2003).
28. G. F. Lorusso and L. Grella, "Undercut measurement using SEM," U.S. patent 6,670,612 B1 (30 December 2003).
29. K. Murayama, S. Gonda, H. Koyanagi, T. Terasawa, and S. Hosaka, "Critical-dimension measurement using

multi-angle-scanning method in atomic force microscope," Jpn. J. Appl. Phys. **45**, 5928–5932 (2006).
30. K. Murayama, S. Gonda, H. Koyanagi, T. Terasawa, and S. Hosaka, "Side-wall measurement using tilt-scanning method in atomic force microscope," Jpn. J. Appl. Phys. **45**, 5423–5428 (2006).
31. N. G. Orji and R. G. Dixson, "Higher order tip effects in traceable CD-AFM-based linewidth measurements," Meas. Sci. Technol. **18**, 448–455 (2007).
32. X. P. Qian and J. S. Villarrubia, "General three-dimensional image simulation and surface reconstruction in scanning probe microscopy using a dexel representation," Ultramicrosc. **108**, 29–42 (2007).
33. X. P. Qian, J. Villarrubia, F. L. Tian, and R. Dixson, "Image simulation and surface reconstruction of undercut features in atomic force microscopy," Proc. SPIE **6518**, 651811 (2007).
34. J. Opsa, H. Y. Chu, Y. X. Wen, Y. C. Chang, and G. W. Li, "Fundamental solutions for real-time optical CD metrology," Proc. SPIE **4689**, 163–176 (2002).
35. R. Subramanian, B. Singh, and K. A. Phan, "Using scatterometry to detect and control undercut for ARC with developable BARCs," U.S. patent 6,972,201 B1 (6 December 2005).
36. J. Lee, P. Im, Y. Park, and J. Kim, "Welding bead and chamfer inspection by means of laser vision," Proc. SPIE **4190**, 41–50 (2001).
37. A. W. Williams and N. J. Wood, "Photothermal imaging of damage and undercutting to gold-coated Kapton samples exposed to atomic oxygen," Opt. Laser Technol. **28**, 469–476 (1996).
38. D. Nyyssonen and Chris P. Kirkt, "Optical microscope imaging of lines patterned in thick layers with variable edge geometry: theory," J. Opt. Soc. Am. A **5**, 1270–1280 (1988).
39. J. W. Liu and G. K. Fedder, "Silicon undercut characterization in a CMOS-MEM process," in *International Solid-State Sensors, Actuators and Microsystems Conference, 2007/Transducers 2007* (IEEE, 2007), pp. 505–508.
40. C. Kaiser, Y. Levy, T. Tiedje, J. F. Young, and I. Kelson, "Determining the profile of textured membranes by the alpha particle energy loss method," Appl. Phys. Lett. **80**, 2607–2609 (2002).
41. K. Legacy, "Industrial CT scanning speeds mold qualification," Plast. Technol. (2008), http://www.ptonline.com/articles/200809fa2.html.
42. I. J. Stares, C. Duffill, J. A. Ogilvy, and C. B. Scruby, "On-line weld pool monitoring and defect detection using ultrasonics," NDT Int. **23**, 195–200 (1990).
43. M. H. Lu, "Imaging thin film structures by scanning acoustic microscopy," U.S. patent application 20080022774 A1 (31 January 2008).
44. F. Guilak, "Volume and surface area measurement of viable chondrocytes in situ using geometric modelling of serial confocal sections," J. Microsc. **173**, 245–256 (1994).
45. "LSM 510 and LSM 510 META Laser Scanning Microscopes," Operating Manual (Carl Zeiss, 2002).
46. S. G. Li, Z. G. Xu, I. Reading, S. F. Yoon, Z. P. Fang, and J. H. Zhao, " Three dimensional sidewall measurements by laser fluorescent confocal microscopy," Opt. Express **16**, 4001–4014 (2008).
47. http://homepages.inf.ed.ac.uk/rbf/HIPR2/gsmooth.htm.
48. G. J. Yang and T. S. Huang, "The effect of median filtering on edge location estimation," Comput. Graph. Image Process. **15**, 224–245 (1981).
49. L. C. Kuypers, W. F. Decraemer, J. J. J. Dirckx, and J.-P. Timmermans, "A procedure to determine the correct thickness of an object with confocal microscopy in case of refractive index mismatch," J. Microsc. **218**, 68–78 (2005).
50. D. Bucher, M. Scholz, M. Stetter, K. Obermayer, and H.-J. Pflüger, "Correction methods for three-dimensional reconstructions from confocal images. I. Tissue shrinking and axial scaling," J. Neurosci. Methods **100**, 135–143 (2000).
51. A. Egner, M. Schrader, and S. W. Hell, "Refractive index mismatch induced intensity and phase variations in fluorescence confocal, multiphoton and 4Pi-microscopy," Opt. Commun. **153**, 211–217 (1998).
52. H. J. Van Elburg, L. C. Kuypers, W. F. Decraemer, and J. J. J. Dirckx, "Improved correction of axial geometrical distortion in index-mismatched fluorescent confocal microscopic images using high-aperture objective lenses," J. Microsc. **228**, 45–54 (2007).
53. A. Diaspro, F. Federici, and M. Robello, "Influence of refractive-index mismatch in high-resolution three-dimensional confocal microscopy," Appl. Opt. **41**, 685–690 (2002).
54. S. G. Li, T. Thorsen, Z. G. Xu, Z. P. Fang, J. H. Zhao, and S. F. Yoon, "Microvalve thickness and topography measurements in microfluidic devices by white light confocal microscopy," Appl. Opt. **48**, 5088–5094 (2009).
55. M. J. Booth and T. Wilson, "Refractive-index-mismatch induced aberrations in single-photon and two-photon microscopy and the use of aberration correction," J Biomed. Opt. **6**, 266–272 (2001).
56. O. Haeberlé, M. Ammar, H. Furukawa, K. Tenjimbayashi, and P. Török, "Point spread function of optical microscopes imaging through stratified media," Opt. Express **11**, 2964–2969 (2003).
57. H. Jacobsen and S. W. Hell, "Effect of the specimen refractive index on the imaging of a confocal microscope employing high aperture oil immersion lenses," Bioimaging **3**, 39–47 (1995).
58. P. Török, "Focusing of electromagnetic waves through a dielectric interface by lenses of finite Fresnel number," J. Opt. Soc. Am. A **15**, 3009–3015 (1998).
59. http://en.wikipedia.org/wiki/Wetting.
60. http://en.wikipedia.org/wiki/Dimethyl_sulfoxide.
61. A. Marmur, "Wetting on hydrophobic rough surfaces: to be heterogeneous or not to be?," Langmuir **19**, 8343–8348 (2003).
62. S.-K. Chae, C.-H. Lee, S. H. Lee, T.-S. Kima, and J. Y. Kang, "Oil droplet generation in PDMS microchannel using an amphiphilic continuous phase," Lab Chip **9**, 1957–1961 (2009).